INL/EXT-17-43374 Rev. 0

September 2017

Microstructure-Level Modeling of Stage 3 Fission Gas Release in UO_2 Fuel

Larry Aagesen
Daniel Schwen
Yongfeng Zhang

INL/EXT-17-43374 Rev. 0

Microstructure-Level Modeling of Stage 3 Fission Gas Release in UO_2 Fuel

Larry Aagesen
Daniel Schwen
Yongfeng Zhang

September 2017

Idaho National Laboratory
Fuels Modeling and Simulation Department
Idaho Falls, Idaho 83415

Prepared for the
U.S. Department of Energy
Office of Nuclear Energy
Under U.S. Department of Energy-Idaho Operations Office
Contract DE-AC07-99ID13727

ABSTRACT

A new phase-field model of fission gas bubble evolution was developed and applied to gain an improved understanding of the microstructure-level processes leading to fission gas release from nuclear fuel and to inform improvements to the fission gas release model used in BISON. The phase-field model simulates the evolution of multiple fuel grains and intergranular bubbles simultaneously, tracks the local concentration of vacancies and gas atoms, and includes the effect of hydrostatic gas pressure on the surrounding fuel matrix. This represents the most realistic microstructure-level model of fission gas bubbles developed to date. The model was used to simulate the growth of grain face and grain edge bubbles in a hexagonally periodic 3D grain structure, which contains multiple grain boundaries and triple junctions. The coverage of grain boundaries and triple junctions by fission gas bubbles was calculated as a function of time. Preliminary results suggest that grain edge bubbles do not release a significant amount of gas prior to gas release by grain face bubbles, which supports the assumptions of the fission gas release model currently used in BISON. However, the simulations should be improved by including a physically realistic number of grain edge bubbles in the initial conditions before definitive conclusions can be drawn.

CONTENTS

FIGURES

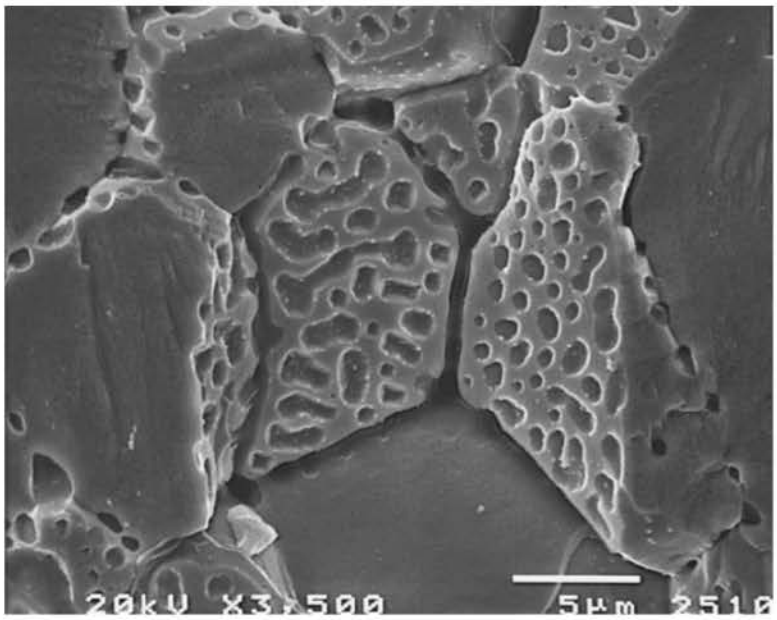

Figure 1: Scanning electron micrograph of grain edge tunnels [1].

1 Introduction

During operation of commercial light water reactors, fission of nuclear fuel results in the formation of a variety of fission products within the fuel matrix. Bubbles of low-solubility fission products, such as the noble gases Xe and Kr, nucleate when gas concentration becomes sufficiently high. Bubbles that form at grain faces (grain boundaries) or grain edges (triple junctions) present a particular concern for operation of light water reactors. As these bubbles grow in size, they eventually form a percolated network. When this network becomes connected to a free surface, the fission gas contained in the bubbles is released to the free volume of the fuel-cladding gap and plenum. The release of the fission gases degrades the thermal conductivity of the fuel-cladding gap, leading to higher fuel centerline temperatures and thus a reduced margin to fuel relocation/melting in accident scenarios. The increase in pressure due to fission gas release also accelerates the degradation of the mechanical properties of the cladding. Due to the negative consequences of fission gas release on fuel performance, a thorough understanding of the mechanisms leading to fission gas release is crucial to ensuring safe operation of commercial light water reactors (LWRs).

The release of fission gas occurs in three stages. In Stage 1, gaseous fission products are produced in the fuel matrix and are transported by diffusion to grain boundaries. In Stage 2, grain face bubbles nucleate and grow on grain boundaries, beginning to interconnect with each other and with grain edges when their size becomes large enough. At the same time, bubbles nucleate, grow, and begin to interconnect on grain edges. In Stage 3, a percolated network of triple junctions is formed, creating tunnels that connect to the fuel outer surface. When percolated grain faces connect to this percolated grain edge network, the gas contained in the grain face bubbles is released. An example of such tunnels formed at grain edges is shown in Figure 1.

Models for the evolution of fission gas bubble microstructure and release processes have been developed in the past using analytical [2, 3, 4, 5, 6] and computational [7, 8, 9, 10, 11, 12] methods. However, due to the complexity of the microstructures formed during Stage 3, few of these models have attempted to include the effects of grain edge bubbles and the need for a percolated pathway to the surface for fission gas release to occur. In spite of past efforts in simulating fission gas

bubble evolution and fission gas release at the microstructural level, INL's engineering-scale fuel performance code, BISON, currently uses an empirical criteria for fission gas release; when the grain boundary fraction coverage reaches 0.5 at any position, the gas at that location is released to the free space between the fuel and cladding [13].

In this work, we apply a phase-field model to investigate the percolation of fission gas bubbles along grain edges. The phase-field model explicitly represents the microstructure of multiple grains and the bubble phase, and thus is well-suited to study the simultaneous evolution of grain face bubbles and grain edge bubbles. Here, we apply a recently developed multi-phase, multi-order parameter, multi-component phase model based on an extension of the grand-potential formulation originally developed by Plapp [14]. Within this model, we have also implemented a new approach to including the hydrostatic gas pressure exerted by the bubbles on the surrounding fuel matrix, which allows the effects of gas pressure on microstructural evolution to be included.

To simulate multiple grains, triple junctions, grain face bubbles, and grain edge bubbles simultaneously, large-scale 3D simulations are required, so the phase-field model must be highly efficient. The model allows the removal of the bulk energy contribution to interfacial energy, allowing increased interface thickness to be used. The increased interface thickness allows the use of a coarser mesh, improving computational efficiency. The model is implemented using the MOOSE framework, allowing use of the framework's inherent capabilities for adaptive meshing, adaptive time stepping using implicit schemes, and parallelization [15]. By applying this model to a polycrystalline microstructure with both grain face bubbles and grain edge bubbles, the evolution of grain edge and grain face coverage can be simultaneously calculated. Comparing the grain face and grain edge coverage as a function of time will allow the determination of a correlation between the two that will be used to inform the development of a more physically-based fission gas release model for BISON.

2 Phase-field model of fission gas bubble evolution

The microstructure of the fuel consists of multiple grains of UO_2 fuel, intragranular gas bubbles, and intergranular gas bubbles. Because intragranular bubbles do not connect to free surfaces, they do not contribute directly to fission gas release. However, the trapping and resolution of fission gas atoms may affect the effective mobility of the gas atoms. For computational efficiency, we do not explicitly include intragranular bubbles in this model, instead encompassing their effect in the diffusion coefficient of gas atoms. In the phase-field model, the microstructure is represented with a set of order parameters. For a microstructure consisting of p grains, the individual grains of the fuel matrix are represented by a set of order parameters $\eta_{m1}, \eta_{m2}, \ldots, \eta_{mp}$. Each fission gas bubble is crystallographically indistinguishable from the others, so the bubbles are represented by a single order parameter η_{b0}. Within grain i of the fuel, $\eta_{mi} = 1$, $\eta_{mj} = 0\ \forall j \neq i$, and $\eta_{b0} = 0$. Within the bubble phase, $\eta_{b0} = 1$ and $\eta_{mj} = 0\ \forall j$.

In addition to the local crystal structure, the local concentration of defect species is also needed to describe the microstructure. We assume that the dominant defect species are U vacancies and fission gas atoms on U lattice sites. Both U vacancies and interstitials are produced by collision cascades; however, interstitials are much more mobile and therefore diffuse to sinks much more rapidly than vacancies. Therefore, there is a net formation of vacancies which can be represented by a source term for net vacancy production. For fission gas atoms on U lattice sites, the formation of bubbles is driven by the low-solubility Xe and Kr atoms. We assume that the properties of the fission gas atoms can be described by the properties of Xe atoms on U sites, since Xe production occurs at a rate nearly ten times that of Kr [16]. The density of vacancies and gas atoms are represented by variables ρ_v and ρ_g, respectively, with units of number of defects per unit volume. These quantities can be converted to the local composition (mole fraction) c of the U lattice using $c = \rho V_a$, where V_a is the atomic volume occupied by a U atom in the UO_2 crystal structure. V_a was calculated to be 0.0409 nm^3 by dividing the unit cell volume of 0.164 nm^3 (calculated from the lattice constant of 0.547 nm [17]) by 4 U atoms in the unit cell.

2.1 Grand potential functional

To derive the evolution equations for the microstructure, the total grand potential Ω of the system is written as a function of the local grand potential density:

$$\Omega = \int_V \left(m \left[\sum_\alpha \sum_{i=1}^{p_\alpha} \left(\frac{\eta_{\alpha i}^4}{4} - \frac{\eta_{\alpha i}^2}{2} \right) + \sum_\alpha \sum_{i=1}^{p_\alpha} \left(\sum_\beta \sum_{j=1, \alpha i \neq \beta j}^{p_\beta} \frac{\gamma_{\alpha i \beta j}}{2} \eta_{\alpha i}^2 \eta_{\beta j}^2 \right) + \frac{1}{4} \right] + \frac{\kappa}{2} \sum_\alpha \sum_{i=1}^{p_\alpha} |\nabla \eta_{\alpha i}|^2 + \sum_\alpha h_\alpha \omega_\alpha \right) dV \tag{1}$$

where α and β are indices for phases, i and j index grains of each phase, p_α and p_β are the number of grains of phase α and β, m is a constant free energy barrier coefficient, κ is the gradient energy coefficient (considered to be independent of interface orientation and misinclination here), and the set of parameters $\gamma_{\alpha i \beta j}$ allows the adjustment of interfacial energies between phases and grains. ω_α is the local grand potential density of each phase, and h_α is an switching function for phase α that has value $h_\alpha = 1$ in phase α and $h_\alpha = 0$ in all other phases. The switching function was introduced in Ref. [18] and has the form

$$h_\alpha = \frac{\sum_{i=1}^{p_\alpha} \eta_{\alpha i}^2}{\sum_\beta \sum_{i=1}^{p_\beta} \eta_{\beta i}^2} \tag{2}$$

For the matrix and bubble phases, the switching functions reduce to

$$h_m = \frac{\sum_{i=1}^{p} \eta_{mi}^2}{\eta_{b0} + \sum_{i=1}^{p} \eta_{mi}^2} \tag{3}$$

$$h_b = \frac{\eta_{b0}}{\eta_{b0} + \sum_{i=1}^{p} \eta_{mi}^2} \tag{4}$$

The grand potential density for each phase is given by

$$\omega_m = f_m - \mu_g \rho_g - \mu_v \rho_v \tag{5}$$

$$\omega_b = f_b - \mu_g \rho_g - \mu_v \rho_v \tag{6}$$

where f_m and f_b are the Helmholtz free energies of each phase and μ_g and μ_v are the chemical potentials of the gas atoms and vacancies, respectively. The Helmholtz free energies are given by

$$f_m = f_{m,chem} + f_{m,el} \tag{7}$$

$$f_b = f_{b,chem} + f_{b,el} \tag{8}$$

where $f_{m,chem}$ and $f_{b,chem}$ are the chemical energy contributions and $f_{m,el}$ and $f_{b,el}$ is the elastic energy contributions.

2.2 Chemical energy contribution and parameterization

The bulk chemical free energy density of the matrix phase, $f_{m,chem}$, is considered first. The solid phase free energy is parameterized using the approach of Ref. [11]. Assuming that the chemical energy of the matrix can be approximated as an ideal solution, the Helmholtz free energy density is written

$$\begin{aligned} f_{m,ideal} = \frac{1}{V_m}\big\{ & RT[c_v \ln c_v + (1-c_v)\ln(1-c_v)] + N_A E_v^f c_v \\ & + RT[c_g \ln c_g + (1-c_g)\ln(1-c_g)] + N_A E_g^f c_g \big\} \end{aligned} \tag{9}$$

where V_m is the molar volume, R is the ideal gas constant, $V_m = V_a N_A$, N_A is Avogadro's number, E_v^f is the formation energy of a U vacancy, and E_v^g is the formation (incorporation) energy of a gas (Xe) atom on a U lattice site. As in Ref. [11], we assume $E_v^f = 3$ eV and $E_g^f = 3$ eV, and use $T = 1200$ K as a temperature representative of LWR operation (numerical parameters are summarized in Table 1). To simplify the numerical solution of the governing equations, $f_{m,ideal}$ was approximated with a parabolic function:

$$f_{m,chem} = \frac{1}{2} k_v^m (c_v - c_v^{m,eq})^2 + \frac{1}{2} k_g^m (c_g - c_g^{m,eq})^2 \tag{10}$$

where k_v^m and k_g^m are the curvatures of the parabolas and $c_v^{m,eq}$ and $c_g^{m,eq}$ are the equilibrium composition of vacancies and gas atoms in the UO_2 matrix. The equilibrium compositions are determined from the formation energies and temperature using $c_v^{m,eq} = \exp(-E_v^f / k_B T)$ and $c_g^{m,eq} = \exp(-E_g^f / k_B T)$. The curvatures of the parabolas are set by assuming that at the steady-state vacancy composition during reactor operation, c_v^0, the chemical potential determined from the parabolic approximation is equal to the chemical potential of the ideal solution model. Since $\mu = \frac{\partial f}{\partial \rho} = \frac{\partial f}{\partial c}\frac{\partial c}{\partial \rho} = V_a \frac{\partial f}{\partial c}$,

$$V_a \left.\frac{\partial f_{m,chem}}{\partial c_v}\right|_{c_v^0} = V_a \left.\frac{\partial f_{m,ideal}}{\partial c_v}\right|_{c_v^0} \tag{11}$$

This leads to an expression for k_v^m, assuming $c_v^0 = 0.01$ as in Ref. [11]:

$$k_v^m = \frac{1}{(c_v^0 - c_v^{m,eq})}\left[\frac{RT}{V_m}[\ln c_v^0 - \ln(1 - c_v^0)] + \frac{N_A E_v^f}{V_m}\right] = 4.81 \times 10^{11}\ \mathrm{J/m^3} \tag{12}$$

We also assume $c_g^0 = 0.01$ as in Ref. [11], and thus $k_g^m = k_v^m$.

The bulk chemical free energy density of the gas bubble phase, $f_{b,chem}$, is considered next. The bubble phase is considered to be a mixture of vacancies and gas atoms with no U atoms present. For intergranular bubbles, it is assumed that the bubbles are not overpressurized relative to equilibrium, so their composition can be determined from the condition of chemical equilibrium. The bubble phase can be treated as a van der Waals gas [16], in which the gas atoms are assumed to have a hard-sphere exclusion volume characterized by the parameter b. For Xe, $b = 0.085\ \mathrm{nm^3/atom}$ [16]. (Due to the high density of Xe atoms in bubbles, the long-range attractive interactions in the van der Waals gas are neglected.) The chemical free energy density of the bubble phase is given by the Helmholtz free energy density of a van der Waals gas:

$$f_{b,vdW} = n_g kT\left[\ln\left(\frac{1}{n_Q\left(\frac{1}{n_g} - b\right)}\right) - 1\right] + f_0 \tag{13}$$

where n_g is the number density of gas atoms, $n_Q = \left(\frac{mk_BT}{2\pi\hbar}\right)^{3/2}$ is the quantum concentration, m is the mass of a Xe atom, and f_0 is an offset to ensure that the solid and gas free energies are measured relative to the same reference state. n_g can be put in terms of relevant problem variables using $n_g = c_g n_U$ (where $n_U = 1/V_a$ is the number density of U atoms in the UO_2 lattice) as long as $c_v + c_g = 1$ holds. f_0 is determined by setting the gas and solid phase free energies equal when they are in the same reference state, which is chosen to be the state in which all U sites are occupied by vacancies. In this case, Eq. 9 yields $f_{m,ideal}(c_v = 1, c_g = 0) = E_v^f/V_a = 1.17 \times 10^{10}\ \mathrm{J/m^3}$ for the solid phase. By setting $f_{m,ideal}(c_v = 1, c_g = 0) = f_{b,vdW}(c_v = 1, c_g = 0)$, $f_0 = 1.17 \times 10^{10}\ \mathrm{J/m^3}$.

The free energy of the gas phase can be more easily understood by considering the Gibbs triangle representing the composition of U lattice sites in Figure 2. The corners of the triangle represent 100% U atoms, vacanices, and Xe atoms, and are labeled accordingly. The corner corresponding to 100% vacancies is the reference state for measuring the solid and gas phase free energies, as discussed in the previous paragraph. Along the edge linking the Xe and Vac corners, no U is present, so $c_v + c_g = 1$. Thus, along that edge, the Helmholtz free energy of the gas phase is given by Eq. (13). A plot of Eq. (13) along that edge is also shown in Figure 2.

As seen in Fig. 2, $f_{b,vdW}$ increases dramatically when $c_g > 0.49$. This occurs as $\frac{1}{n_g} - b$ approaches 0, and corresponds physically to the density at which the volume occupied by a Xe atom approaches the hard sphere exclusion volume b. By setting $\frac{1}{n_g} - b = \frac{1}{c_g n_U} - b = 0$, it can be determined that $f_{b,vdW} \to \infty$ as $c_g \to 0.494$. To simplify numerical calculations, for phase-field simulations a parabolic approximation was fit to the Helmholtz free energy:

$$f_{b,chem} = \frac{1}{2}k_v^b(c_v - c_v^{b,eq})^2 + \frac{1}{2}k_g^b(c_g - c_g^{b,eq})^2 + f_{min} \tag{14}$$

The minimum of the parabolic free energy was set to occur at the minimum of the van der Waals free energy, resulting in $c_g^{b,eq} = 0.454$, $c_v^{b,eq} = 0.546$. This composition is found along the Vac-Xe edge of the Gibbs triangle in Fig. 2. To match the value of minimum of the van der Waals free energy, $f_{min} = 9.54 \times 10^9\ \mathrm{J/m^3}$. Because composition in the gas bubbles will generally not deviate far from the minimum of the free energy, k_v^b and k_g^b were set by assuming $k_v^b = k_g^b$ and fitting to $f_{b,vdW}$ in the range $0.42 < c_g < 0.49$, resulting in $k_v^b = k_g^b = 9.0 \times 10^{10}\ \mathrm{J/m^3}$.

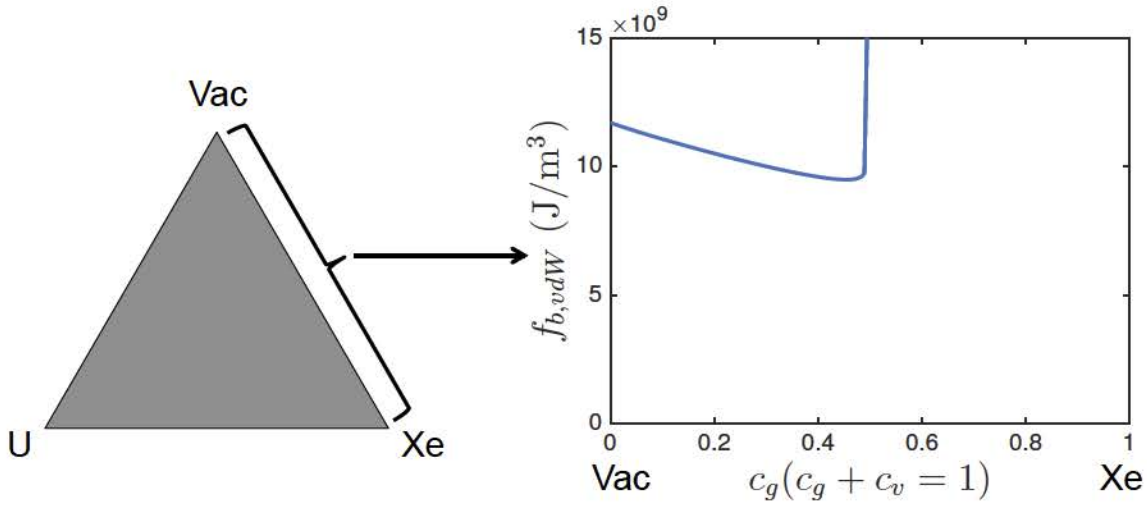

Figure 2: Left, the Gibbs triangle representation of composition of the U lattice sites. The corners correspond to 100% U atoms, vacancies, and Xe atoms. Along the Vac-Xe edge, no U atoms are present, so $c_g + c_v = 1$. Right, the Helmholtz free energy of the gas phase is plotted along the Vac-Xe edge using Eq. (13), with $c_g = 0$ corresponding to the pure vacancy corner and $c_g = 1$ corresponding to the pure Xe corner.

2.3 Interfacial energy and parameterization

In Ref. [19], the grain boundary energies for UO_2 were calculated for a variety of grain boundary types and misorientations. Based on these results, the grain boundary energy can be approximated as isotropic with a value of $\sigma_{mm} = 1.5$ J/m^2. The semi-dihedral angle of a grain boundary bubble is determined by the balance of grain boundary energy and bubble-matrix interfacial energy using Young's equation. In UO_2, the semi-dihedral angle is approximately 50°, resulting in a bubble-matrix interfacial energy of $\sigma_{mb} = 1.17$ J/m^2. The phase-field model is parameterized so that these interfacial energies are accurately represented.

Using the grand potential functional of Eq. (1), the interfacial energy $\sigma_{\alpha i \beta j}$between grain i of phase α and grain j of phase β is given by [20, 18]

$$\sigma_{\alpha i \beta j} = g(\gamma_{\alpha i \beta j})\sqrt{\kappa m} \tag{15}$$

where $g(\gamma_{\alpha i \beta j})$ is a dimensionless function of γ that in general must be evaluated numerically. However, for the special case $\gamma = 1.5$, $g(\gamma = 1.5) = \sqrt{2}/3$. Here, we choose the interface between any grain i of the matrix phase and grain j of the matrix phase to have $\gamma_{mimj} = 1.5$. For this special case, analytical expressions can be used that relate κ and m to the interfacial energy and characteristic thickness l_{int} of the interface [20, 18]:

$$\kappa = \frac{3}{4}\sigma_{mm} l_{int} \tag{16}$$

$$m = \frac{6\sigma_{mm}}{l_{int}} \tag{17}$$

To resolve the intergranular bubbles, l_{int} is chosen to be 30 nm, and $\sigma_{mm} = 1.5$ J/m^2, resulting in $\kappa = 3.38 \times 10^{-8}$ J/m and $m = 3.00 \times 10^8$ J/m^3. To control the bubble-matrix interfacial energy, since κ and m are fixed, the parameters γ_{mib0} must be determined to obtain the correct value of

σ_{mb}, which is assumed to be constant and isotropic. To determine the value of γ_{mib0}, using Eq. (15),

$$\sigma_{mb} = g(\gamma_{mib0})\sqrt{\kappa m} \tag{18}$$

$$\sigma_{mm} = g(\gamma_{mimj})\sqrt{\kappa m} \tag{19}$$

Dividing Eq. (18) by Eq. (19),

$$\frac{\sigma_{mb}}{\sigma_{mm}} = \frac{g(\gamma_{mib0})}{g(\gamma_{mimj})} \tag{20}$$

Rearranging Eq. (20),

$$g(\gamma_{mib0}) = g(\gamma_{mimj} = 1.5)\frac{\sigma_{mb}}{\sigma_{mm}} = \frac{\sqrt{2}}{3}\frac{1.17}{1.5} = 0.367 \tag{21}$$

A polynomial approximation has been fit to numerical results that allows γ to be found as a function of g [21]:

$$\gamma = \left(-5.288g^8 - 0.09364g^6 + 9.965g^4 - 8.813g^2 + 2.007\right)^{-1} \tag{22}$$

Using this approximation, $\gamma_{mib0} = 0.922$.

2.4 Elastic energy and parameterization

The hydrostatic pressure in the fission gas bubbles is exerted on the surrounding fuel matrix, resulting in elastic energy in the fuel. This elastic energy contributes to Eq. (1) and therefore influences microstructural evolution. To incorporate fission gas bubble pressure into the phase-field models, an equivalent inclusion approach has been used in the past for simulations of spherical intragranular bubbles [11]. However, the equivalent inclusion approach requires the calculation of the Eshelby tensor [22]. Though this is feasible for ellipsoidal shapes, to our knowledge a solution to the Eshelby tensor for the lenticular shape of intergranular bubbles does not exist. Thus, we have developed a new approach to including hydrostatic gas pressure in bubbles with arbitrary shape, as detailed in this section.

The elastic energy contributes to the Helmholtz free energy of each phase, as shown in Eq. (7) - (8). $f_{m,el}$ has the usual form for a linear elastic solid:

$$f_{m,el} = \frac{1}{2}\sigma_{ij}^m \epsilon_{ij} \tag{23}$$

where σ_{ij}^m is the stress tensor in the matrix and ϵ_{ij} is the strain tensor, defined as

$$\epsilon_{ij} = \frac{1}{2}\left(\frac{\partial u_i}{\partial x_j} + \frac{\partial u_j}{\partial x_i}\right) \tag{24}$$

where u_i is ith component of displacement and x_i is the ith coordinate direction. The stress tensor for the matrix phase has a linear elastic constitutive law

$$\sigma_{ij}^m = C_{ijkl}^m \epsilon_{kl} \tag{25}$$

where C_{ijkl}^m is the stiffness tensor for UO_2. The components of the stiffness tensor were taken from Ref. [23] and are shown in Table 1.

For the gas phase, we assume it can be treated as a highly compliant solid, as has been done previously in phase-field modeling of solid-gas systems [24, 25, 26]. The elastic energy is given by

$$f_{b,el} = \frac{1}{2}\sigma_{ij}^b \epsilon_{ij} \tag{26}$$

The stress field in the bubble phase σ_{ij}^b is given by the hydrostatic pressure of the gas phase plus a small contribution from a linear elastic constitutive law:

$$\sigma_{ij}^b = \sigma_{ij}^g + C_{ijkl}^b \epsilon_{kl} \tag{27}$$

The contribution from the linear elastic constitutive law ensures that the displacement field does not become strongly discontinuous through the solid-gas interface. To ensure that it gives a negligible contribution to elastic energy, we set $C_{ijkl}^b = 10^{-4} C_{ijkl}^m$. The stress tensor from the gas pressure σ_{ij}^g is related to the hydrostatic pressure in the bubble P as

$$\sigma_{ij}^g = \begin{cases} -P & i = j \\ 0 & i \neq j \end{cases} \tag{28}$$

Although in principle the gas pressure varies with the bubble phase gas composition c_g, we assume that for intergranular bubbles, c_g will not deviate significantly from its value at the minimum of the gas free energy curve in Fig. 2, and thus that P can be approximated as a constant set by the pressure corresponding to $c_g^{b,eq} = 0.454$. From the data of Ref. [27], at $c_g = 0.454$, $P = 465$ MPa. This is close to the experimentally measured intergranular gas pressures reported in Ref. [28], validating the approach.

To solve for the displacement fields, the mechanical equilibrium equation must be solved simultaneously with the evolution equations. In the weak form, the mechanical equilibrium equation is

$$\int_V w_{i,j} \sigma_{ij} dV = 0 \tag{29}$$

where the w_i is the ith finite element shape function, and $w_{i,j}$ is the derivative of the ith shape function in the jth direction. To calculate the stress tensor at each position in Eq. (29), we interpolate the stress tensor for each phase using the previously defined interpolation functions h_m and h_b:

$$\sigma_{ij} = h_b \sigma_{ij}^b + h_m \sigma_{ij}^m \tag{30}$$

This scheme, in which the strain is assumed constant between phases in the interface and the stress is interpolated as a function of order parameter, has been referred to as the Voight-Taylor scheme and has been previously applied in phase-field modeling [29, 30, 31, 32].

2.5 Evolution equations

From the grand potential functional of Eq. (1), the Allen-Cahn equations for evolution of the order parameters can be derived:

$$\begin{aligned} \frac{\partial \eta_{\alpha i}}{\partial t} &= -L \frac{\delta \Omega}{\delta \eta_{\alpha i}} \\ \frac{\partial \eta_{\alpha i}}{\partial t} &= -L \left[m \left(\eta_{\alpha i}^3 - \eta_{\alpha i} + 2\eta_{\alpha i} \sum_{\beta} \sum_{j=1, \alpha i \neq \beta j}^{p_\beta} \gamma_{\alpha i \beta j} \eta_{\beta j}^2 \right) \right. \\ &\qquad \left. - \kappa \nabla^2 \eta_{\alpha i} + \sum_{\alpha} \frac{\partial h_\alpha}{\partial \eta_{\alpha i}} \omega_\alpha \right] \end{aligned} \tag{31}$$

where $\frac{\delta \Omega}{\delta \eta_{\alpha i}}$ is the variational derivative of Ω with respect to order parameter $\eta_{\alpha i}$ and L is the order parameter mobility, which is general is a function of order parameters and concentration. Parameterization of L will be discussed later in this section.

To evolve the gas and vacancy concentrations, it will be more convenient to write the evolution equations in terms of chemical potentials μ_v and μ_g and use the chemical potentials as the field variables rather than compositions. To enable this, the grand potentials in each phase, Eq. (5) - (6), must be expressed in terms of μ_v and μ_g for use in Eq. (31). For the matrix phase, the relation $\mu_g = V_a \frac{\partial f_{m,chem}}{\partial c_g} = V_a k_g^m (c_g - c_g^{m,eq})$ can be re-arranged to yield

$$c_g = \frac{\mu_g}{V_a k_g^m} + c_g^{m,eq} \tag{32}$$

Similarly,

$$c_v = \frac{\mu_v}{V_a k_v^m} + c_v^{m,eq} \tag{33}$$

Eq. (32) - (33) can be used in conjunction with $\rho_g = \frac{c_g}{V_a}$, $\rho_v = \frac{c_v}{V_a}$, Eq. (5), (7), and (10) to obtain the grand potential density as a function of chemical potentials rather than concentrations:

$$\omega_m = -\frac{1}{2}\frac{\mu_v^2}{V_a^2 k_v^m} - \frac{\mu_v}{V_a} c_v^{m,eq} - \frac{1}{2}\frac{\mu_g^2}{V_a^2 k_g^m} - \frac{\mu_g}{V_a} c_g^{m,eq} + f_{m,el} \tag{34}$$

Similarly, the grand potential density of the bubble phase can be expressed as

$$\omega_b = -\frac{1}{2}\frac{\mu_v^2}{V_a^2 k_v^b} - \frac{\mu_v}{V_a} c_v^{b,eq} - \frac{1}{2}\frac{\mu_g^2}{V_a^2 k_g^b} - \frac{\mu_g}{V_a} c_g^{b,eq} + f_{b,el} \tag{35}$$

The evolution equations for μ_g and μ_v are

$$\frac{\partial \mu_g}{\partial t} = \frac{1}{\chi_g}\left[\nabla \cdot (D_g \chi_g \nabla \mu_g) + s_g - \sum_\alpha \sum_{i=1}^{p_\alpha} \frac{\partial \rho_g}{\partial \eta_{\alpha i}} \frac{\partial \eta_{\alpha i}}{\partial t}\right] \tag{36}$$

$$\frac{\partial \mu_v}{\partial t} = \frac{1}{\chi_v}\left[\nabla \cdot (D_v \chi_v \nabla \mu_v) + s_v - \sum_\alpha \sum_{i=1}^{p_\alpha} \frac{\partial \rho_v}{\partial \eta_{\alpha i}} \frac{\partial \eta_{\alpha i}}{\partial t}\right] \tag{37}$$

where χ_g and χ_v are the susceptibilities, D_g and D_v are the diffusion coefficients, and s_g and s_v are the source terms for production of Xe atoms and U site vacancies.

The source term $s_g = s_g^0 h_m$ is given by a constant rate of Xe production, s_g^0, times the switching function h_m, which has a value of 1 in the fuel matrix and 0 inside the bubble. This is to limit production of new Xe atoms to the fuel matrix in the model. The Xe production rate $s_v^0 = \dot{F} Y_{Xe}$, where $\dot{F}$ is the fission rate density and Y_{Xe} is the fission yield of Xe. $\dot{F}$ is estimated to be 1.09×10^{13} fissions/(cm^3 s) based on typical operating values for a light water reactor [16]. Y_{Xe} is taken to be 0.2156 based on the thermal neutron Xe yield for U-235 [33]. The vacancy production rate is similarly given by $s_v = s_v^0 h_m$. s_v^0 is not known, so it is varied parametrically in the range s_g^0 to $20 s_g^0$, and the effect of this parameter on grain boundary coverage and grain edge coverage is studied.

The susceptibility χ describes the relationship between solute density and its chemical potential: $\chi = \frac{\partial \rho}{\partial \mu}$ [14]. This relationship differs based on the phase of the system, so χ is interpolated based on the local phase using the switching functions h_α. For gas atoms,

$$\chi_g = h_m \chi_g^m + h_b \chi_g^b \tag{38}$$

where $\chi_g^m = \frac{\partial \rho_g^m}{\partial \mu_g}$ and $\chi_g^b = \frac{\partial \rho_g^b}{\partial \mu_g}$. Since the governing equations are in terms of the chemical potentials, the susceptibilities must also be expressed in terms of chemical potentials, which can

be done as follows. Using $\rho_g^m = \frac{c_g}{V_a}$, and substituting for c_g using Eq. (32), $\chi_g^m = \frac{\partial \rho_g^m}{\partial \mu_g} = \frac{1}{V_a^2 k_g^m}$. Similar expressions can be derived for χ_v^m, χ_g^b, and χ_v^b, resulting in

$$\chi_g = h_m \frac{1}{V_a^2 k_g^m} + h_b \frac{1}{V_a^2 k_g^b} \tag{39}$$

$$\chi_v = h_m \frac{1}{V_a^2 k_v^m} + h_b \frac{1}{V_a^2 k_v^b} \tag{40}$$

The diffusion coefficient for Xe, D_g, was set to 0.1 nm^2/s based on experimental measurement in stoichiometric UO_2 [34]. The diffusion coefficient for U vacancies, D_v, was set to the same value.

The governing equations are non-dimensionalized using length scale $l^* = 1$ nm, time scale $\tau^* = 0.1$ s, and energy density scale $E^* = C_{1212} = 64 \times 10^9$ J/m^3. Finally, we describe the parameterization of the order parameter mobility L. In the simulation configuration used, the grain boundaries between fuel matrix grains are static, and the change in microstructure is only due to the motion of matrix-bubble interfaces. We therefore use a constant L for all interfaces, and set L throughout based on the matrix-bubble interfaces. We assume that the motion of the bubble-matrix interface is limited by diffusion, and thus set the non-dimensionalized order parameter mobility $\bar{L}$ high enough that interface motion was diffusion-limited. $\bar{L} = 0.1$ was chosen based on the fact that further increases did not result in changes to the microstructure. To convert this to a dimensional value, since the dimensions of L are volume/(energy $\times$ time), $L = \frac{\bar{L}}{E^* \tau^*}$. This is equivalent to a dimensional value $L = 1.56 \times 10^{-11}$ $\text{m}^3/(\text{J s})$.

The non-dimensionalized governing equations were discretized using the MOOSE framework [15]. Hexahedral 3D mesh elements with linear Lagrange shape functions were used for spatial discretization. Mesh adaptivity was used, with three levels of refinement and a minimum element size of $\Delta x = \Delta y = \Delta z = 10$ nm. Periodic boundary conditions were used in all directions. The second-order backward differentiation formula was used for time integration, and adaptive time stepping was used with the MOOSE IterationAdaptiveDT time stepper, with eight optimal nonlinear iterations and an iteration window of two.

Parameter	Value
T	1200 K
V_a	0.0409 nm^3
E_v^f	3 eV
E_v^g	3 eV
$c_g^{b,eq}$ (intergranular)	0.3924
$c_v^{b,eq}$ (intergranular)	0.6076
$k_v^m = k_g^m$	4.81×10^{11} $\mathrm{J/m}^3$
$k_v^b = k_g^b$	9.0×10^{10} $\mathrm{J/m}^3$
f_{min}	9.54×10^{9} $\mathrm{J/m}^3$
κ	3.38×10^{-8} J/m
m	3.00×10^{8} $\mathrm{J/m}^3$
γ_{mimj}	1.5
γ_{mib0}	0.922
C_{1111}^m	395 GPa
C_{1122}^m	121 GPa
C_{1212}^m	64 GPa
P	465 MPa
$\dot{F}$	1.09×10^{13} fissions/(cm^3 s)
Y_{Xe}	0.2156
s_g^0	2.35×10^{12} atoms/(cm^3 s)
D_g	0.1 nm^2/s
D_v	0.1 nm^2/s
L	1.56×10^{-11} $\mathrm{m}^3/(\mathrm{J\ s})$

Table 1: Parameters used for phase-field simulations.

3 Phase-field Simulation Results

3.1 Initial Conditions

To simulate the growth of grain edge and grain face bubbles simultaneously, a grain structure with both grain boundaries and triple junctions is required, and a 3D domain is required for triple junctions. However, this must be balanced against the need for a simulation domain small enough to be computationally tractable. To balance these requirements, a 2D periodic structure of four uniform hexagonal grains in the x-y plane is extended in the z-direction. This structure has eight triple junctions parallel to the z-direction. Because all grain boundaries are flat, this configuration is metastable with respect to grain growth, allowing the evolution of fission gas bubble microstructure to be studied independently of grain boundary motion.

The hexagons in the grain structure in these simulations have an edge-to-edge distance d of 0.6 μm. This is smaller than the typical grain size of ~ 5 μm in UO_2 in commercial LWRs. However, assuming that the areal density N_A of fission gas bubbles at the early stages of bubble formation is approximately $20/\mu m^2$ [6]), the characteristic spacing between bubbles is $l = 1/\sqrt{N_A} = 0.224$ μm, smaller than the grain size. This configuration is therefore large enough to allow a reasonable number of bubbles to be placed on the grain boundaries and grain edges, and to allow the growth of grain face bubbles onto grain edges to be simulated. The size of the simulation domain in the x, y, and z directions is defined as L_x, L_y, and L_z, respectively. $L_x = 2d = 1.2$ μm for the hexagonal geometry. It can be shown that for the uniform hexagons, $L_y = \sqrt{3}L_x/2 = 1.04$ μm. L_z is chosen to be 0.48 μm. The grain boundary area for this configuration without bubbles is $A_{GB} = 2\sqrt{3}L_xL_z = 2$ μm^2. Based on $N_A = 20$ μm^2, 40 bubbles are placed on the grain boundaries in the simulation initial conditions, and one grain edge bubble is placed. The bubbles in the initial conditions are spherical with a radius of 44 nm; at the beginning of the simulation, the bubbles rapidly equilibrate to their expected lenticular shape.

3.2 Microstructural evolution

The evolution of the microstructure for a simulation with $s_v^0 = 5s_g^0$ is shown in Figure 3. Grain boundaries are shown in semitransparent blue, and fission gas bubbles are shown in yellow. In the early stages of evolution, grain face bubbles have begun to take the expected lenticular shape, as seen in Fig. 3a. The shape of grain edge bubbles is approximately triangular in cross-section and begins to expand along the z-direction. A few bubbles have begun to coalesce. As time progresses, grain face bubbles grow and more coalescence occurs, see Figure 3b - 3c. The grain boundaries remain in their initial metastable configuration, as expected. The grain edge bubble begins to elongate along the z-direction, beginning the process of grain edge tunnel formation. In Figure 3c, it can be seen that grain boundary bubbles that were initially close to a grain edge grow preferentially toward and onto the grain edge, demonstrating a mechanism that causes grain edge coverage to increase more rapidly than grain boundary coverage. At the end of the simulation time, 1157 days (Figure 3d), the grain edges have been completely covered by gas bubbles, while the grain faces are 62% covered by bubbles.

3.3 Grain boundary coverage and triple junction coverage

The grain boundary coverage and the triple junction coverage were calculated as a function of time from the phase-field simulations. The grain boundary coverage X_{GB} is defined as the projected area of the bubbles onto the grain boundaries, A_b, divided by the original grain boundary area of

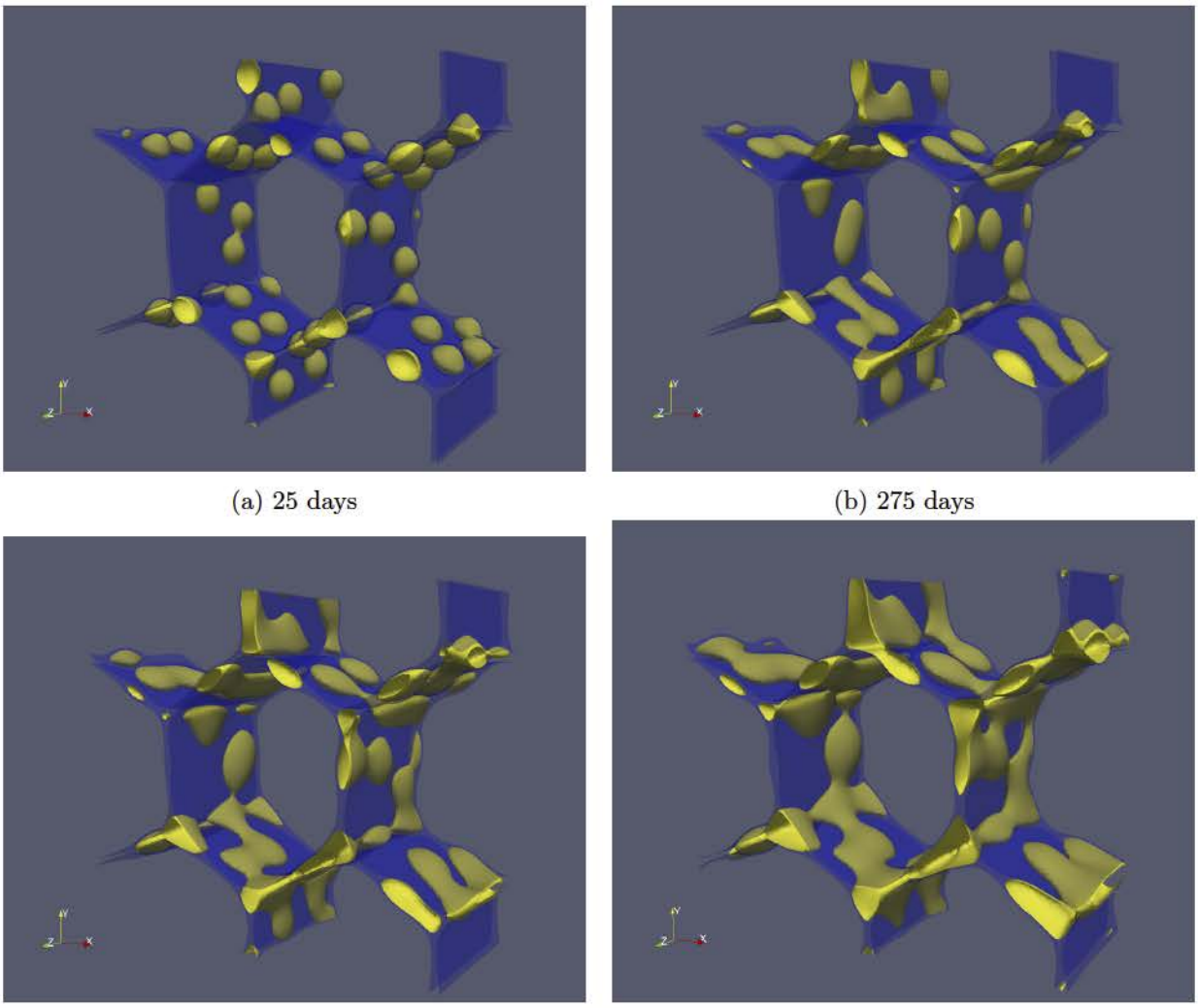

(a) 25 days

(b) 275 days

(c) 586 days

(d) 1157 days

Figure 3: Evolution of microstructure with $s_v^0 = 5s_v^0$. The grain boundaries are shown in semi-transparent blue and the gas bubbles are shown in yellow.

the hexagonal grain configuration in the absence of bubbles, A_{GB}. The trijunction coverage X_{TJ} is defined as the projected length of the bubbles onto the trijunctions, L_b, divided by the total length of the trijunctions, which for this configuration is equal to $8L_z$. X_{GB} and X_{TJ} are plotted as a function of time in Figure 4 for vacancy source strengths of $s_v^0 = s_g^0$, $5s_g^0$, and $20s_g^0$. (The microstructural images shown in Figure 3 correspond to the data in Figure 4c - 4d.)

Comparing the results of Fig. 4a-f, there is a rapid increase in grain boundary coverage at very early times for all vacancy source strengths considered. This occurs as the spherical bubbles in the initial conditions rapidly take their expected lenticular shape by expanding along the grain boundaries. The initial trijunction coverage does not increase as rapidly in the early stages, due to the different morphology of the trijunction bubble. However, within a relatively short time after this initial transient, trijunction coverage begins to increase faster than grain boundary coverage. This is due to two effects. The first is the growth of grain boundary bubbles toward grain edges, as discussed in Section 3.2. The second is that vacancies and gas atoms will preferentially migrate toward grain edge bubbles rather than grain boundary bubbles due to their flatter interfaces and

therefore lower chemical potentials. For the lowest s_v^0 considered, $s_v^0 = s_g^0$, the trijunctions are not fully percolated ($X_{TJ} = 1$) at the end of the simulation. However, for $s_v^0 = 5s_g^0$ and $s_v^0 = 20s_g^0$, the trijunctions become fully percolated.

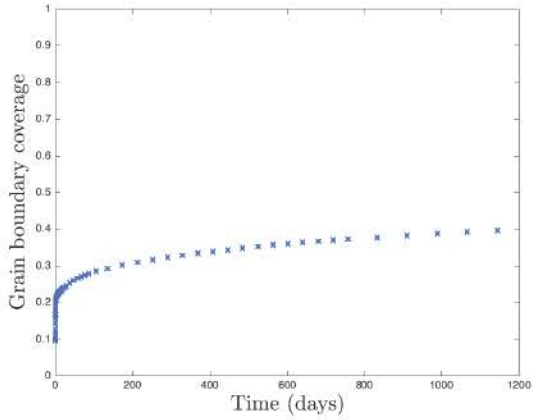

(a) $s_v^0 = s_g^0$

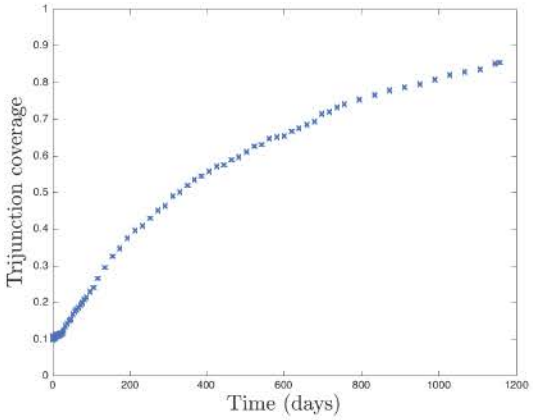

(b) $s_v^0 = s_g^0$

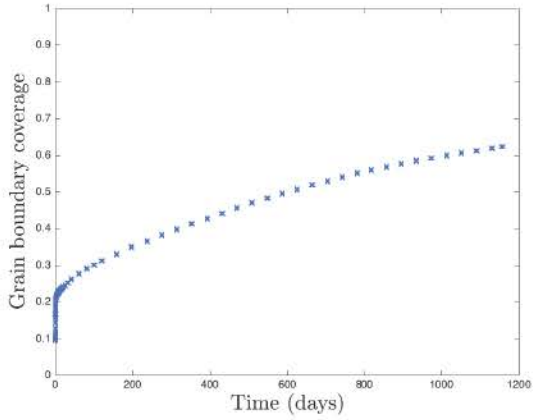

(c) $s_v^0 = 5s_g^0$

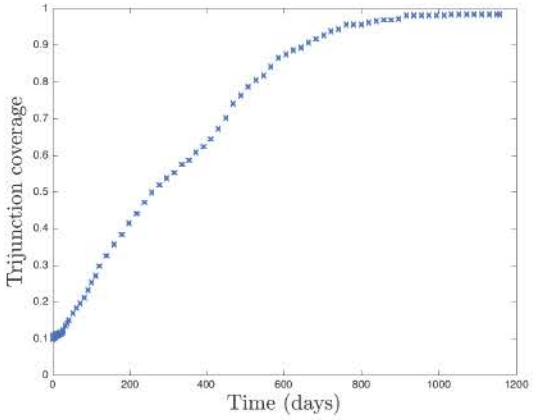

(d) $s_v^0 = 5s_g^0$

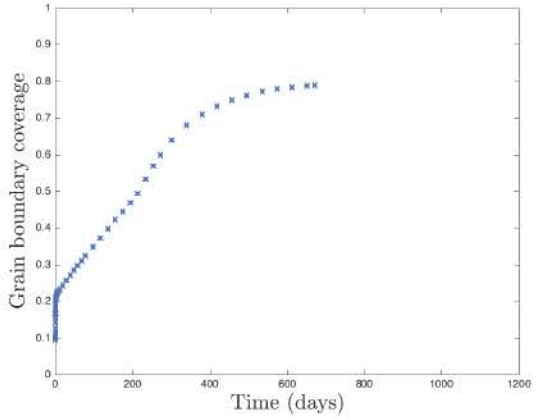

(e) $s_v^0 = 20s_g^0$

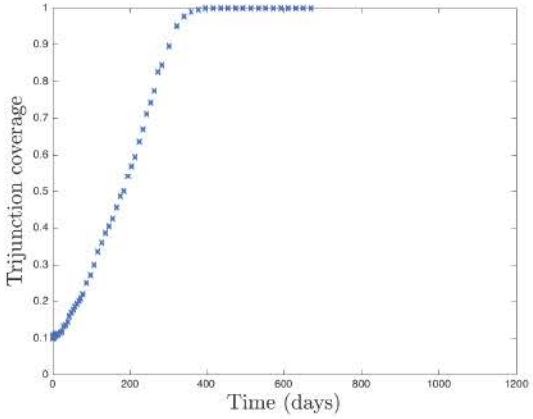

(f) $s_v^0 = 20s_g^0$

Figure 4: Evolution of grain boundary coverage and trijunction coverage as a function of time, for varying vacancy source strength s_v^0. (The microstructural images shown in Figure 3 correspond to the data in Figure 4c - 4d.)

4 Discussion

An important question to consider from these simulations is how they can inform the fission gas release criteria used in BISON. In BISON, gas release occurs as soon as $X_{GB} = 0.5$, and there is no consideration of the need for a percolated path to the surface [13]. This criteria is based on observations of X_{GB} from experiment [6], and is consistent with the trends observed by Millett et al. [8], who found with phase-field simulations that the fraction of grain boundaries that was vented increased sharply in the range $0.4 < X_{GB} < 0.6$. Figure 4 shows that X_{TJ} does not reach 1 before $X_{GB} = 0.5$ for any of the vacancy production rates considered, meaning that the triple junctions do not become percolated before the grain faces. However, this is not consistent with experimental observations [1]. This discrepancy may be due to the fact that the probability of nucleation of grain edge bubbles relative to grain face bubbles has not been adequately considered in the initial conditions of these simulations. This is due to the lack of data, experimental or computational, on the number density of grain edge versus grain face bubbles for any burnup. To definitely conclude whether the BISON fission gas release criteria should be revised, a method to estimate the number of grain edge bubbles for the given number of grain face bubbles in the initial conditions should be developed in future work.

5 Conclusions

Fission gas release has potentially negative consequences for fuel performance in light water reactors. To gain an improved understanding of the processes leading to fission gas release, a phase-field model has been used to simulate the growth and interconnection of grain face and grain edge bubbles in UO_2 fuel. The phase-field model is based on a grand-potential functional and allows simulation of multiple grains of fuel and the bubble phase. The solid phase free energies are based on an ideal solution model, while the gas phase free energies are based on the Helmholtz free energy of a van der Waals gas. Parabolic approximations are used for the bulk free energy of each phase. A new approach is developed to include the hydrostatic pressure of the gas phase on the surrounding fuel matrix by adding a constant extra stress dependent on the hydrostatic pressure in the bubble. Source terms are used to include the production of fission gas atoms and the net production of vacancies. This effort represents the most physical model of fission gas bubbles developed to date.

The model is used to simulate the growth of grain face and grain edge bubbles in a hexagonally periodic geometry. The source strength representing the net vacancy production was varied parametrically since its value is unknown. The grain face bubbles have the expected lenticular shape, while the grain edge bubbles have an approximately triangular cross-section. Grain boundary bubbles that were near grain edges in the initial conditions grow preferentially toward the grain edges and thus become grain edge bubbles. The grain boundary coverage and trijunction coverage were calculated and plotted as a function of time. Although the grain boundary coverage increases rapidly at very early times, soon after, trijunction coverage begins to grow more rapidly than grain boundary coverage. At the end of the simulation time, for the higher vacancy source terms, the grain edges are completely percolated.

Ultimately, the objective of this work is to inform the fission gas release model used in BISON. Currently, BISON tracks grain boundary coverage, and allows all gas within a local volume element to be released when grain boundary coverage exceeds 0.5. The phase-field model developed in this work provides a means to validate or refine this criteria. In the current simulations, the trijunction coverage reaches 1 after grain boundary coverage reaches 0.5. However, due to lack of data, the phase-field simulations in this work did not employ initial conditions with a physically justifiable number of grain edge bubbles. In future work, a physically-based estimate of the number of grain edge bubbles in the initial conditions will be developed. This will allow definitive conclusions to be made about the assumptions in the current fission gas release model.

6 References

1. I. Zacharie, S. Lansiart, P. Combette, M. Trotabas, M. Coster, and M. Groos. Microstructural analysis and modelling of intergranular swelling of an irradiated uo2 fuel treated at high temperature. *J. Nucl. Mater.*, 255(2-3):92 – 104, 1998.

2. W. Beere and G. L. Reynolds. Morphology and growth-rate of interlinked porosity in irradiated UO_2. *Journal of Nuclear Materials*, 47(1):51–57, 1973.

3. J. A. Turnbull and M. O. Tucker. Swelling in UO_2 under conditions of gas release. *Philosophical Magazine*, 30(1):47–63, 1974.

4. M. O. Tucker and J. A. Turnbull. The morphology of interlinked porosity in nuclear fuels. *Proceedings of the Royal Society A*, 343(1634):299, 1975.

5. M. O. Tucker. Simple description of interconnected grain edge porosity. *Journal of Nuclear Materials*, 79(1):199–205, 1979.

6. R.J. White. The development of grain-face porosity in irradiated oxide fuel. *Journal of Nuclear Materials*, 325:61–77, 2004.

7. Shenyang Hu, Charles H. Jr., Howard L. Heinisch, Marius Stan, Michael I. Baskes, and Steven M. Valone. Phase-field modeling of gas bubbles and thermal conductivity evolution in nuclear fuels. 392(2):292 – 300, 2009.

8. Paul C. Millett, Michael R. Tonks, S.B. Biner, Liangzhe Zhang, K. Chockalingam, and Yongfeng Zhang. Phase-field simulation of intergranular bubble growth and percolation in bicrystals. *J. Nucl. Mater.*, 425(1):69–76, 2012.

9. P. C. Millett. Percolation on grain boundary networks: Application to fission gas release in nuclear fuels. *Computational Materials Science*, 53(1):31–36, 2012.

10. P. C. Millett, M. R. Tonks, and S. B. Biner. Grain boundary percolation modeling of fission gas release in oxide fuels. *Journal of Nuclear Materials*, 424(1-3):176–182, 2012.

11. Yulan Li, Shenyang Hu, Robert Montgomery, Fei Gao, and Xin Sun. Phase-field simulations of intragranular fission gas bubble evolution in UO2 under post-irradiation thermal annealing. *Nuclear Instruments and Methods in Physics Research Section B: Beam Interactions with Materials and Atoms*, 303:62–67, 2013.

12. D. Sabogal-Suarez, J. D. Alzate-Cardona, and E. Restrepo-Parra. Fission gas bubble percolation on crystallographically consistent grain boundary networks. *Journal of Nuclear Materials*, 475:81–86, 2016.

13. G. Pastore, L. P. Swiler, J. D. Hales, S.R. Novascone, D. M. Perez, B. W. Spencer, L. Luzzi, P. Van Uffelen, and R. L. Williamson. Uncertainty and sensitivity analysis of fission gas behavior in engineering-scale fuel modeling. *Journal of Nuclear Materials*, 456:398–408, 2015.

14. M. Plapp. Unified derivation of phase-field models for alloy solidification from a grand-potential functional. *Physical Review E*, 84(3), 2011.

15. D. Gaston, C. Newman, G. Hansen, and D. Lebrun-Grandié. MOOSE: A parallel computational framework for coupled systems of nonlinear equations. *Nucl. Eng. Design*, 239:1768–1778, 2009.

16. D. R. Olander. *Fundamental aspects of nuclear reactor fuel elements.* Technical Information Center, Energy Research and Development Administration, 1976.

17. M. Idiri, T. Le Bihan, S. Heathman, and J. Rebizant. Behavior of actinide dioxides under pressure: UO_2 and ThO_2. *Physical Review B*, 70(1), 2004.

18. N. Moelans. A quantitative and thermodynamically consistent phase-field interpolation function for multi-phase systems. *Acta Materialia*, 59(3):1077–1086, 2011.

19. Marmot update for oxide fuel modeling. Report INL/EXT-16-40039, Idaho National Laboratory, 2016.

20. N. Moelans, B. Blanpain, and P. Wollants. Quantitative analysis of grain boundary properties in a generalized phase field model for grain growth in anisotropic systems. *Phys. Rev. B*, 78:024113, 2008.

21. http://nele.studentenweb.org/docs/parameters.m; accessed 07-Oct-2016.

22. T. Mura. *Micromechanics of Defects in Solids.* Kluwer Academic Publishers, 1987.

23. J. B. Wachtman, M. L. Wheat, H. J. Anderson, and J. L. Bates. Elastic constants of single crystal UO_2 at 25 degrees c. *Journal of Nuclear Materials*, 16(1):39–41, 1965.

24. J. J. Eggleston and P. W. Voorhees. Ordered growth of nanocrystals via a morphological instability. *Applied Physics Letters*, 80(2):306–308, 2002.

25. S. M. Wise, J. S. Lowengrub, J. S. Kim, and W. C. Johnson. Efficient phase-field simulation of quantum dot formation in a strained heteroepitaxial film. *Superlattices and Microstructures*, 36(1-3):293–304, 2004.

26. S. M. Wise, J. S. Lowengrub, J. S. Kim, K. Thornton, P. W. Voorhees, and W. C. Johnson. Quantum dot formation on a strain-patterned epitaxial thin film. *Applied Physics Letters*, 87(13), 2005.

27. C. Ronchi. Extrapolated equation of state for rare gases at high temperatures and densities. *Journal of Nuclear Materials*, 96(3):314–328, 1981.

28. M. Mogensen, C. Bagger, and C. T. Walker. An experimental study of the distribution of retained xenon in transient-tested UO_2 fuel. *Journal of Nuclear Materials*, 199(2):85–101, 1993.

29. K. Ammar, B. Appolaire, G. Cailletaud, and S. Forest. Combining phase field approach and homogenization methods for modelling phase transformation in elastoplastic media. *European Journal of Computational Mechanics*, 18(5-6):485–523, 2009.

30. A. Durga, P. Wollants, and N. Moelans. Evaluation of interfacial excess contributions in different phase-field models for elastically inhomogeneous systems. *Modelling and Simulation in Materials Science and Engineering*, 21(5), 2013.

31. A. Durga, P. Wollants, and N. Moelans. A quantitative phase-field model for two-phase elastically inhomogeneous systems. *Computational Materials Science*, 99:81–95, 2015.

32. L. K. Aagesen, D. Schwen, K. Ahmed, and M. R. Tonks. Quantifying elastic energy effects on interfacial energy in the Kim-Kim-Suzuki phase-field model with different interpolation schemes. *Computational Materials Science*, in press, 2017.

33. International Atomic Energy Agency. Chain fission yields. https://www-nds.iaea.org/sgnucdat/c1.htm; accessed 13-Apr-2017.

34. W. Miekeley and F. W. Felix. Effect of stoichiometry on diffusion of xenon in UO_2. *Journal of Nuclear Materials*, 42(3):297–306, 1972.